SLAC–PUB–11084
April 2005

Dynamic Aperture in Damping Rings with Realistic Wigglers

Yunhai Cai
Stanford Linear Accelerator Center
Menlo Park, CA 94025

Abstract

The International Linear Collider based on superconducting RF cavities requires the damping rings to have extremely small equilibrium emittance, huge circumference, fast damping time, and large acceptance. To achieve all of these requirements is a very challenging task. In this paper, we will present a systematic approach to designing the damping rings using simple cells and non-interlaced sextupoles. The designs of the damping rings with various circumferences and shapes, including dogbone, are presented. To model realistic wigglers, we have developed a new hybrid symplectic integrator for faster and accurate evaluation of dynamic aperture of the lattices.

Presented at Wiggle 2005 workshop,
Frascati, Italy, February 21-22, 2005

1 Introduction

Nearly all of the existing design of damping rings, including the dogbone design of the TESLA damping ring [1], are based on the theoretical minimum emittance (TME) cell [2] to achieve the required emittance. Contrasted with the FODO cell, the TME cell is much more efficient for obtaining an extremely small emittance. However, its strong focusing nature, combined with tiny dispersion, often leads very strong sextoples that dramatically degrade the dynamic aperture in the rings. As a consequence, when a large acceptance in the positron damping ring is required, an additional damping ring of identical circumference is introduced to stage the reduction of emittance and enlarge the acceptance in a chain of two consecutive rings. For small ring, adding another ring is indeed a cost effective solution to resolve the conflict between the small emittance and large acceptance in the damping system. Therefore, the two-ring scheme is widely adopted in the designs of linear colliders, such as NLC [3].

For the International Linear Collider (ILC), the chosen RF technology, based on superconducting cavities, requires a long train consisting of 2820 bunches equally separated 400 ns. Even with a compression scheme that utilizes an extremely fast (20 ns) kicker, the long train still requires a 17-kilometer circumference ring to store all the bunches and damp their emittance. Clearly, for this kind of huge damping ring, adding another ring of the same size is not an economical solution to enlarge the acceptance. In this paper, we will explore other alternatives to increase the dynamic aperture without an additional ring. A similar study based on a FODO cell and interlaced sextupoles has been carried out by Wolski [4].

The equilibrium beam emittance in a simple electron or positron storage ring can be written as

$$\epsilon_x = C_q F_c \gamma^2 \phi_d^3, \tag{1.1}$$

where $C_q = 55\hbar c/32\sqrt{3}mc^2 = 3.84 \times 10^{-13} m$, ϕ_d is the bending angle in each dipole magnet, and F_c is a dimensionless factor depending only on the cell structure. It is well known[5] that the TME cell is the optimum cell structure that minimizes F_c and its minimum achievable $F_c^{min} = 1/12\sqrt{15}$.

Given an energy ($\gamma = E/mc^2$), it is easy to see from Eq. (1.1) that there are two ways to reduce the emittance, namely by reducing either F_c or ϕ_d. In this paper we concentrate on the effects of decreasing ϕ_d, since the other road naturally leads to the TME cell [1, 6]. First, to keep the total

bending angle to 2π in a ring, the number of cells has to be increased when reducing ϕ_d. Usually, a larger number of cells leads to larger circumference which makes it easier to host the long bunch train. Second, the weaker bend produces smaller dispersion, which leads to stronger sextupoles. The strong sextupoles can degrade the dynamic aperture in the ring. So how can we quantify the effects?

2 A simple storage ring

Let's start with a simple FODO cell since it is well known that it gives excellent dynamic aperture in storage rings. We choose 90^0 phase advance per cell, which gives $F_c = 2.5$, twice as large as the achievable value with any FODO cell. The 90^0 cell also makes it easier to place non-interlaced sextupole pairs (separated in 180^0) in the lattice.

Parameter	Description	Value
E (Gev)	beam energy	5.0
C (m)	circumference	960
ϵ_x (nm-rad)	horizontal emittance	47.23
τ_t (ms)	damping time	41.13
ν_x,ν_y,ν_s	tunes	15.81, 15.68, 0.054
α_c	momentum compaction	6.24×10^{-3}
σ_z (mm)	bunch length	8.90
σ_e/E	energy spread	5.13×10^{-4}
U_0 (Mev)	energy loss per turn	0.79
ξ_x, ξ_y	natural chromaticity	-16.13, -17.71

Table 1: *Parameters of storage ring with* 90^0 *FODO cells.*

A length of the cell of 15 m leads to the maximum β of about 25 m. Similar β functions are implemented in the PEP-II lattices [7, 8]. These lattice functions have been demonstrated to have reasonable values in order to tolerate the multipole errors in the dipole and quadrupole magnets in the arcs. The shape of the accelerator is a racetrack. Each arc consists of 20 regular cells and ends with half-bend dispersion suppressors. To keep the symmetry, we used four matching sections to change tunes and matched between the dispersion suppressors and 90^0 cells at the middle of the straights. The main

parameters of the ring are tabulated in Table 1 and its lattice functions are calculated using MAD [9] and plotted in Fig. 1.

The natural chromaticity is compensated for by two families of interleaved sextupoles next to the quadrupoles in the arcs. Since every four 90^0 cells make a second-order achromat, all driving terms of the third-order resonances generated by the sextupole are cancelled within each arc, which consists of 20 cells. For the RF system, we used parameters similar to those in B-factories[10, 11]. Its frequency and voltage are 500 MHz and 10 MV respectively.

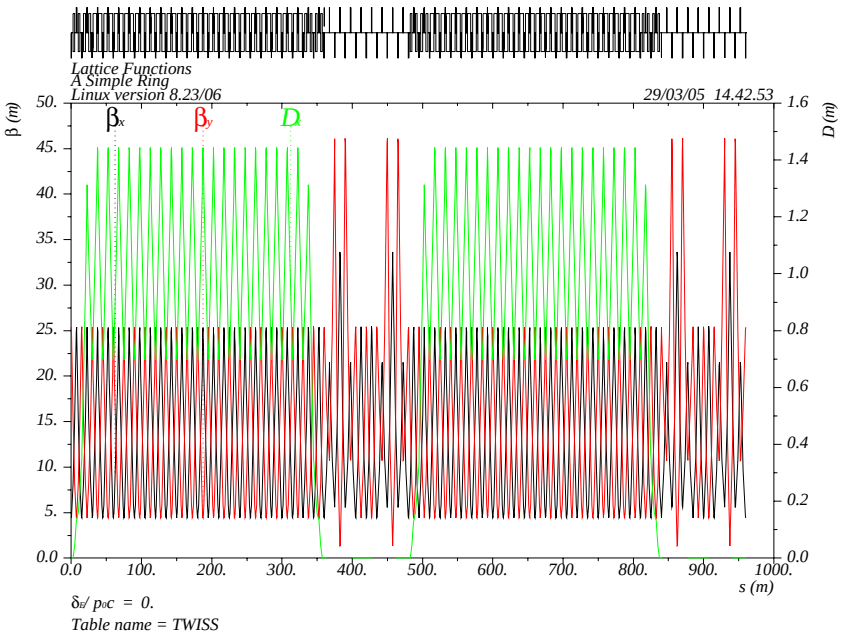

Figure 1: *Lattice functions in a storage ring.*

3 Phase advance in straights

As we mentioned in the previous section, the betatron phase advances in the arcs are locked in order to cancel the excitation of the third-order resonances. The phase advance in the straight is still a free parameter for optimizing the dynamic aperture. We can vary the phase by inserting additional 90^0 cells

at the middle of the straights. The resulting changes in dynamic aperture are shown in Fig. 2 in a sequence of the phase change: 0^0, 90^0, 180^0, and 360^0 in the both planes. Shown in plot (b), the best phase advances in the straight section are nearly a multiple of 360^0, which makes the whole straight section an identity transformation and therefore maximizes the symmetry of the ring and minimizes the number of excited high-order resonances. One can clearly see in the plot that the optimized dynamic aperture is nearly 20 $\sigma_{\rm inj}$ (assuming that the injected positron beam has emittance of $\epsilon_x^{inj} = \epsilon_y^{inj} = 1000$ nm-rad).

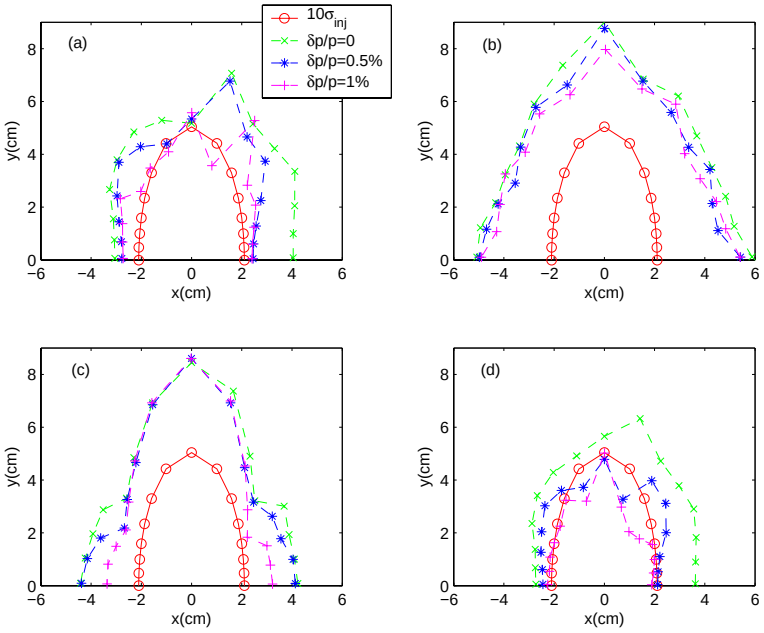

Figure 2: *Dynamic aperture vs. phase advances in straights.*

The dynamic apertures were obtained by tracking particles in 1024 turns with synchrotron oscillations starting with various initial transverse amplitudes and momenta $\delta = 0$, 0.5% and 1.0% using a six-dimensional symplectic tracking code LEGO [12].

4 Scaling of dynamic aperture

In this storage ring, 20 σ_{inj} dynamic aperture is more than sufficient for the acceptance. But its equilibrium emittance ($\epsilon_x = 47$ nm-rad) is still too large

to qualify as a damping ring. As we discussed in the introduction, we need to know how the dynamic aperture degrades as the emittance gets reduced and the sextupoles become stronger. This storage ring provides us an elegant and yet simple way to study this effect. By simply inserting a multiple of four 90^0 cells, which is a unit transformation, in the straight section, we varied the tune and natural chromaticity of the ring without changing the fractional part of the tune. Then we changed the two families of sextupoles in the arcs to correct the total chromaticity to zero. Since the sextupole strengthes are linearly proportional to the tunes of the ring, the arc sextupoles became stronger as we inserted more cells into the straight sections.

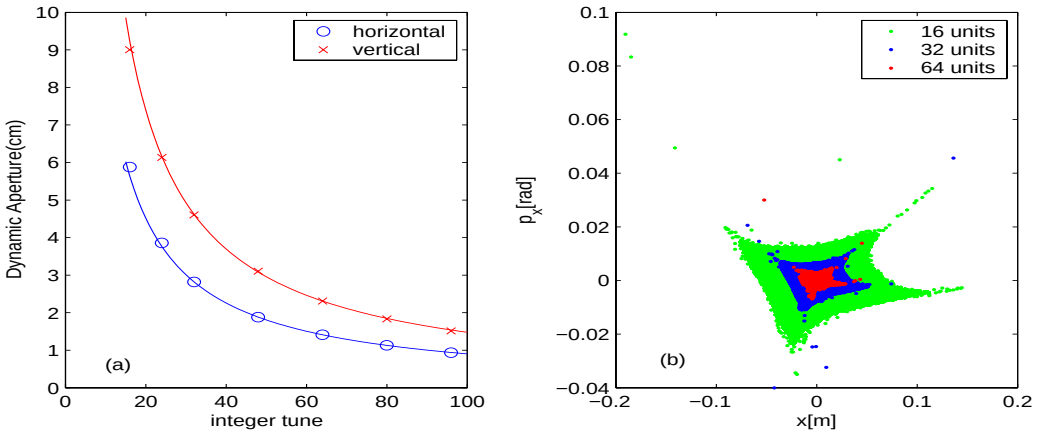

Figure 3: *Scaling property of dynamic aperture with respect to strength of sextupoles. a) the circles and crosses represent the calculated dynamic apertures in stretched rings and the solid lines are the one parameter fit to the inverse function. b) The dots represent the particles that survived 1024 turns in the tracking.*

The result of the study is summarized in Fig. 3: Clearly, the dynamic aperture is inversely proportional to the strength of the sextupoles. And this simple scaling property can be explained by perturbation theory when the dynamic aperture is determined by the location of fixed points in the phase space dominated by a single resonance.

5 Reduce emittance

Based on Eq. (1.1) and the scaling property of the dynamic aperture, found in the last section, we expect the beam emittance and lattice parameters scaled as the following:

$$\begin{cases} \epsilon_x \rightarrow \epsilon_x/8, & \text{(horizontal emittance)} \\ \phi_d \rightarrow \phi_d/2, & \text{(bending angle)} \\ N_c \rightarrow 2N_c, & \text{(number of cells)} \\ \rho_d \rightarrow 2\rho_d, & \text{(bending radius)} \\ \eta_x \rightarrow \eta_x/2, & \text{(horizontal dispersion)} \\ K_{SF,SD} \rightarrow 2K_{SF,SD}, & \text{(strength of sextupole)} \\ DA- > DA/2. & \text{(dynamic aperture)} \end{cases}$$

Here we have assumed that the cell structure (determined by the quadrupole magnets and the space between them) and the length of the dipole are kept the same as the ring is enlarged.

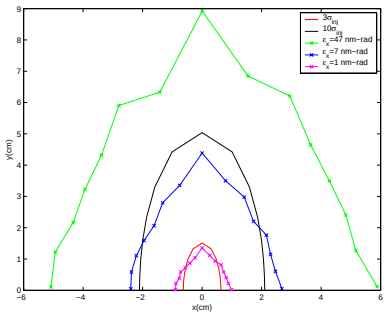

Figure 4: *Dynamic apertures in three rings scaled to reducing the emittance ($\epsilon_x = 47$, 7, and 1 nm-rad).*

According to the scaling law, two additional rings, doubling the number of arc cell N_c from 40 to 80 and then 160, are designed. We found that the emittance ϵ_x is reduced from 47 to 7 and then to 1 nm-rad while the circumference C is increased correspondingly from 960 to 1560 and then to 2760 m. The slight deviation from the scaling law is largely due to the fact that the actual lattices contain dispersion suppressors and straight sections. The dynamic apertures of all three rings are shown Fig 4. One can see that the dynamic apertures dropped a factor of two in each step and behaved just as we expected from the scaling law. Unfortunately, the dynamic aperture has degraded downward to 3 $\sigma_{\rm inj}$ in the largest ring with 1 nm-rad emittance.

6 Non-interlaced sextupoles

There are still two obvious problems to make this 160-cell ring into a damping ring for ILC. First, the damping time is too long because we have weakened the bending dipole to reduce the emittance. Second, the dynamic aperture is not quite adequate.

The damping time can be easily reduced by introducing damping wigglers. To achieve a 21 ms damping time, we add 24 wigglers distributed in twelve 90^0 cells in the straight sections. Each wiggler has 10 periods and is 4-meters long. Its peak field reaches 1.68 T. Because of faster damping, the wigglers further reduce the emittance down to 0.3 nm-rad.

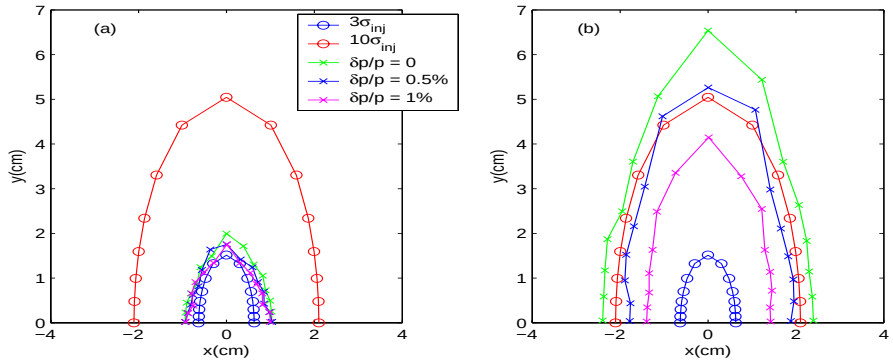

Figure 5: *Comparison between two sextupole schemes: a) interlaced and b) non-interlaced in a compact damping ring based on a FODO cell.*

Since we already arranged the sextupoles in each arc to cancel the excitation of all third-order resonances, the dynamic aperture reduction we saw in the last section can only be caused by the high-order effects generated from the concatenation among the sextupoles. The only known way[13] to eliminate this interference is to pair two sextupoles with an $-I$ transformer without any sextupole in between. This arrangement is called the non-interlaced sextupole scheme, which has been implemented and demonstrated in the B-factories [8, 11] as an effective method of correcting chromaticity and providing adequate dynamic aperture. Incidentally, the non-interlaced arrangement of sextupoles also requires many cells and a large circumference of the ring. For the ring with 160 cells, that is not a problem. Here, we regroup two families of sextupoles into a non-interlaced pattern. The resulting dynamic aperture is significantly improved as shown in Fig. 5.

Due to the sparse arrangement, the non-interlaced sextupoles are three times stronger than the interlaced ones. This implies that the alignment tolerance of the sextupoles becomes much tighter and some kind of beam-based alignment may be necessary in the actual accelerator. The main parameters of the design are listed in Table 2.

Parameter	Description	Value
E (Gev)	beam energy	5.0
C (m)	circumference	2820
ϵ_x (nm-rad)	horizontal emittance	0.3
τ_t (ms)	damping time	21
ν_x,ν_y,ν_s	tunes	47.81, 47.68, 0.016
α_c	momentum compaction	6.0×10^{-4}
σ_z (mm)	bunch length	22.0
σ_e/E	energy spread	1.3×10^{-3}
U_0 (Mev)	energy loss per turn	4.5
ξ_x, ξ_y	natural chromaticity	-60.0, -60.0

Table 2: *Parameters of a compact damping ring with* 90^0 *FODO cells.*

In the table, the bunch length $\sigma_z = 22$ mm is too long compared with the 6 mm achieved in the DESY dogbone damping ring. In order to solve this problem, one can significantly increase the RF voltage [4] or modify the FODO cell to reduce the momentum compaction factor.

7 Detuned π cell

We would like to retain most properties of a FODO cell. The simplest way to reduce the momentum compaction factor is to remove some dipoles in cells without changing the cell structure. An obvious option is to choose a so-called π cell , which was studied during the design stage[14] of KEKB. Basically, a π cell is made of two 90^0 cells with two missing dipoles. The bending angles of the two remaining dipoles are doubled to maintain the total bending in the original two cells. Its optical functions are plotted in Fig. 6. One can see in the figure that the dispersion is minimized at the location of the dipoles, which results in a factor of two reduction in the momentum compaction factor compared with the 90^0 FODO cell.

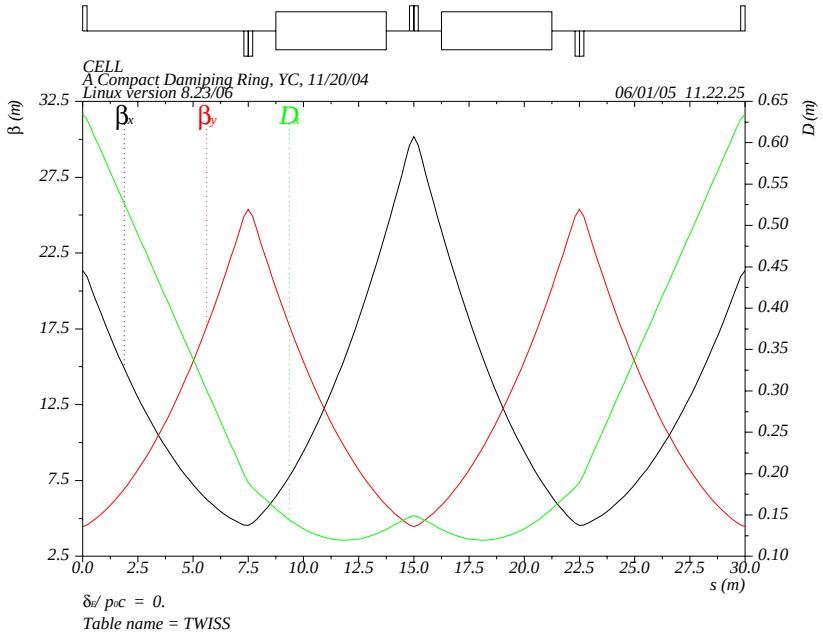

Figure 6: *Lattice functions of a detuned π cell.*

Again, this cell has nearly the same focusing properties as the FODO cell. As a result, the dynamic aperture does not change much compared with FODO lattices. Here, its phase advance is reduced by 1^0 away from 180^0 to improve the dynamic aperture.

8 A compact damping ring

Finally, we completed a design of a compact damping ring based on the detuned π cell and non-interlaced sextupoles scheme. The ring consists of 80 cells in two arcs, four dispersion suppressors, and nearly 100 meter wigglers in two straight sections. The main parameters are tabulated in Table 3.

We found that the sextupole pairs placed at the middle of the cells, where the dispersion is very small, are necessary to retain adequate dynamic aperture for off-momentum particles. They are about a factor four stronger than the pairs near the ends to compensate for the difference of the dispersion.

The bunch length $\sigma_z = 8.3$ mm is easily reduced to 6 mm by increasing the RF voltage from 10 to 12 MV. For a 500 MHz RF system, the harmonic number is 4700. Clearly, there are enough buckets to store 2820 bunches in

Parameter	Description	Value
E (Gev)	beam energy	5.0
C (m)	circumference	2820
ϵ_x (nm-rad)	horizontal emittance	0.49
τ_t (ms)	damping time	20
ν_x,ν_y,ν_s	tunes	47.81, 47.68, 0.021
α_c	momentum compaction	2.83×10^{-4}
σ_z (mm)	bunch length	8.3
σ_e/E	energy spread	1.27×10^{-3}
U_0 (Mev)	energy loss per turn	4.70
ξ_x, ξ_y	natural chromaticity	-60.0, -60.0

Table 3: *Parameters of a compact damping ring with detuned π cells.*

the ring. Of course, the smaller bunch space implies that we will need much a faster kicker for extraction. We can easily stretch the straight sections to make the ring a little larger and store all bunches in every two buckets. That makes that the bunch spacing equal 4 ns. If one can make a 4-ns kicker, this design of a compact damping ring should be seriously considered.

9 A dogbone damping ring

Given a 20-ns kicker, we have to extend this compact ring to a skinny dogbone with a 17-km circumference. Immediately, we face two competing effects. First, when a ring is stretched in straight sections, increased chromaticity results in stronger sextupoles in the arcs. That degrades dynamic aperture as we have shown in Sec. 4. Second, to achieve the same damping time in a much longer ring requires many more damping wigglers. Since the damping wigglers also reduce the emittance, these extra wigglers allow us to relax the emittance, generated by the bending cell in the arcs, to a larger value. That leads to a large dynamic aperture. These two effects on the dynamic aperture of on-momentum particles roughly cancelled each other. For the off-momentum particles, the dynamic aperture in the dogbone ring is worse, largely because of a lack of symmetry.

Similar to the DESY design [1], we use each arc to bend the beam 240^0 positively and then 60^0 negatively to close the ring. Given this geometric constraint, there are a few discrete solutions to configure cells. To achieve the

parameters similar to those in the DESY design, we select the configuration that contains 35 positive bending π cells, 8 negative bending cells, and 4 half-bend dispersion suppressors in each arc. Finally, to retain the two-fold symmetry in the ring, we placed two joins of the dogbone on the opposite side of the parallel long straights. The layout of the ring is shown in Fig. 7

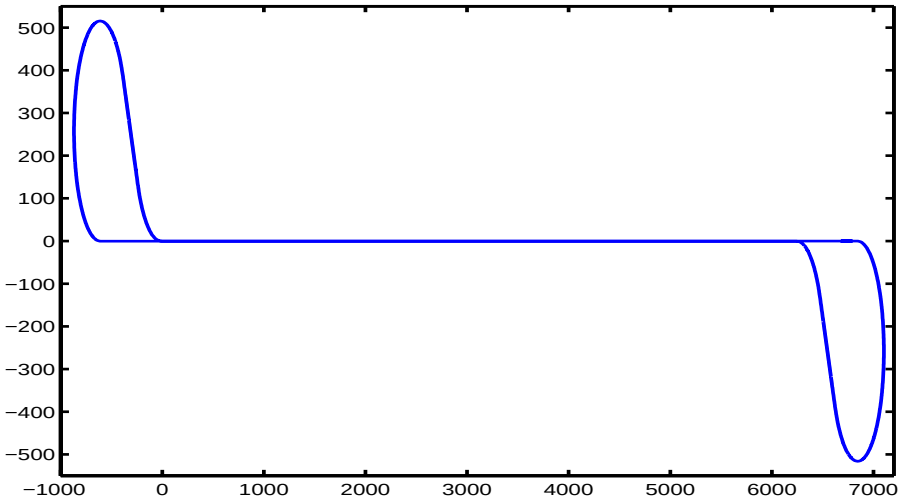

Figure 7: *Layout of the dogbone damping ring.*

Aside from regular cells, dispersion suppressors, and wiggler cells, the ring contains long and weakly focusing cells in straight sections to cover most of the distance and a few matching sections. The parameters of both the DESY ring and the new dogbone ring are listed in Table 4 for comparison. Almost all parameters of the two rings are identical except the betatron tunes and the natural chromaticity. The different type of cell used, one TME and another π cell, explains the difference.

The dynamic apertures of both ring using "linear wigglers", approximated with segmented dipoles, are shown in Fig. 8. The scales of the two plots are different because of difference in β functions at the position where the tracking particles are launched. One can still compare the results by referring to the beam size of the injected beam ($\epsilon_x = \epsilon_y = 1000$ nm-rad). Clearly, the newly designed ring has significantly improved the dynamic aperture. But its dynamic aperture for the off-momentum particles may require further optimization. This improvement may be accomplished by using every pair of sextupoles as an independent family.

Parameter	DESY	SLAC
Energy E (Gev)	5.0	5.0
Circumference C (m)	17000	17014
Emittance ϵ_x (nm-rad)	0.5	0.62
Damping time τ_t (ms)	28	27
Tunes ν_x,ν_y,ν_s	76.31, 41.18, 0.071	83.73, 83.65, 0.072
Momentum compaction α_c	1.22×10^{-4}	1.11×10^{-4}
Bunch length σ_z (mm)	6.04	5.90
Energy spread σ_e/E	1.29×10^{-3}	1.30×10^{-3}
Chromaticity ξ_x, ξ_y	-125, -62.5	-105.27, -106.70
Energy loss per turn U_0 (Mev)	20.4	21.0
RF voltage V_{RF} (MV)	50	50

Table 4: *Parameters of two dogbone damping rings.*

For the dogbone ring, the number of wigglers has been increased to 112 to reduce the damping time. Since actual wigglers are intrinsically nonlinear due to the variation of their magnetic fields, how much nonlinearity can the ring tolerate? Before we can answer this question, we need to know how to describe the magnetic field of a wiggler and then how to integrate through the field.

10 Intrinsic field

In Cartesian coordinate, the intrinsic magnetic field of a wiggler can be derived from a scalar potential that satisfies the Laplace's equation and be written as

$$\begin{aligned} B_y &= \sum_{n=1}^{N_s} B_y^{(n)} \cosh(k_s^{(n)} y) \sin(k_s^{(n)} s + \phi_y^{(n)}), \\ B_s &= \sum_{n=1}^{N_s} B_y^{(n)} \sinh(k_s^{(n)} y) \cos(k_s^{(n)} s + \phi_y^{(n)}]), \end{aligned} \tag{10.1}$$

and $B_x = 0$, where $k_s^{(n)} = (2n-1)k_w$, $k_w = 2\pi/\lambda_w$, and λ_w is the period of the wiggler. Each mode, described by an amplitude $B_y^{(n)}$ and phase $\phi_y^{(n)}$, independently satisfies Maxwell's equation in vacuum:

$$\nabla \cdot \vec{B} = 0, \nabla \times \vec{B} = 0. \tag{10.2}$$

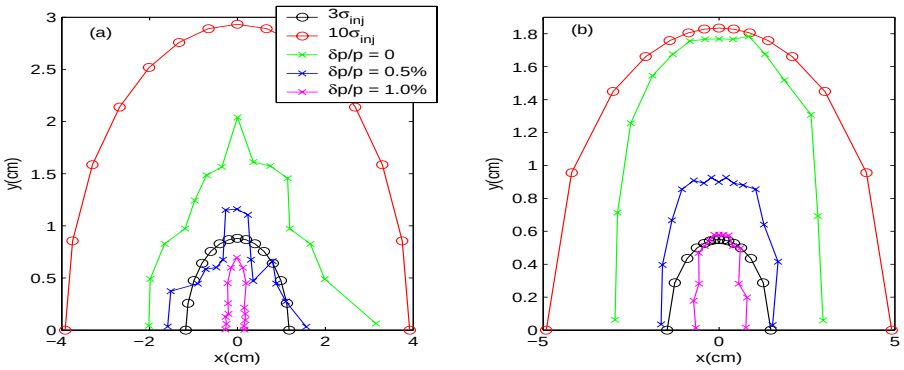

Figure 8: *Dynamic apertures of both dogbone damping rings with linear wigglers: a) DESY's design b) SLAC's new design.*

This property ensures that a finite expansion of harmonics in Eq. (10.1) does not violate Maxwell's equations.

Its vector potential, defined by $\vec{B} = \nabla \times \vec{A}$, can be easily derived in the axial gauge: $A_s = 0$. It can be written as

$$A_x = \sum_{n=1}^{N_s} -(B_y^{(n)}/k_s^{(n)}) \cosh(k_s^{(n)} y) \cos(k_s^{(n)} s + \phi_y^{(n)}), \tag{10.3}$$

and $A_y = 0$. Note that the only non-vanishing component, A_x, does not depend on the coordinate x. This makes the integration much simpler, which will be discussed in the next section. Incidentally, this vector potential also satisfies the Coulomb gauge condition: $\nabla \cdot \vec{A} = 0$.

11 Symplectic integrator

Under the small-angle approximation, the Hamiltonian that describe the motion of a charged particle in a static magnetic field is given by [15]

$$H(x, p_x, y, p_y, \delta, l; s) = -(1+\delta) + \frac{1}{2(1+\delta)}[(p_x - a_x)^2 + (p_y - a_y)^2] - a_s, \tag{11.1}$$

where $\vec{a} = e\vec{A}(x, y, s)/cp_0$. Since H explicitly depends on s, we have to integrate through the system in many segments. Using the notation of Lie algebra, we can write it formally as

$$e^{-\int :H:ds} \approx \prod_{i=1}^{n} e^{-:H(s_i):\Delta s}, \tag{11.2}$$

where Δs is the length of the segment. In each integration step, we can split $H(s_i)$ into three exactly solvable parts:

$$\begin{cases} H_0 = -(1+\delta) + \frac{1}{2(1+\delta)}(p_x^2 + p_y^2), & \text{(drift)} \\ H_1 = \frac{1}{2(1+\delta)}(a_x^2 + a_y^2) - a_s, & \text{(kick)} \\ H_2 = -\frac{1}{(1+\delta)}(p_x a_x + p_y a_y). & \text{(special case)} \end{cases}$$

H_2 is explicitly solvable for the case of the intrinsic field because it does not depend on the coordinate x and thus has an extra constant of motion p_x. As a result of the splitting, a second-order integrator:

$$e^{-:H(s_i):\Delta s} = e^{-\frac{:H_0:}{2}\Delta s} e^{-\frac{:H_1:}{2}\Delta s} e^{-:H_2:\Delta s} e^{-\frac{:H_1:}{2}\Delta s} e^{-\frac{:H_0:}{2}\Delta s} + O(\Delta s^3), \qquad (11.3)$$

can be used to approximate the integration in each step. This kind of integrators can be easily derived [16] by applying the Baker-Cambell-Hausdorf formula. It is obvious that the solution becomes an exact one at the limit of an infinite number of segments. It also preserves the symplecticity during the integration since each Lie factor is symplectic.

12 Effect of single-mode wigglers

For simplicity, let's investigate a single-mode wiggler that has only the first mode: $n = 1$ in Eqs. (10.1) and (10.3). In this simplified case, we apply the second-order symplectic integrator in Eq.(11.3) for the integration of the wiggler selected according to the DESY's design: period $\lambda_w = 0.4$ m, peak field $B_0 = 1.68$ T, and 10 periods. To center the wiggled orbit inside the wiggler, we replace the half pole at both ends with a full pole with a period $\lambda_w/2$ and the same peak field B_0. The centered orbit and dispersion are plotted in Fig 9. Moreover, we found that the wiggled orbit caused an increase of path length of 40 microns in the 4-meter wiggler.

This single-mode wiggler is implemented in LEGO to replace the linear wiggler in both dogbone lattices that have been discussed in previous sections. The linear tune shift of the vertical tune, caused by the substitution, is barely noticeable and therefore it needs not to be compensated with quadrupoles. The total tune shift, including the nonlinear one, caused by the wiggling field can be calculated using the Hamiltonian perturbation theory. Starting from the vector potential in Eq.(10.3) and the Hamiltonian in Eq. (11.1), we find

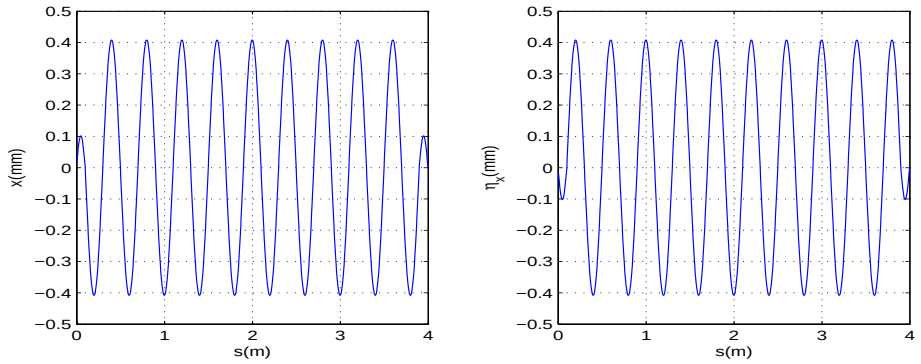

Figure 9: *Wiggled orbit and dispersion inside a wiggler.*

that, for a single-mode wiggler with N_p periods, the tune shift is given by

$$\Delta\nu_y = \frac{N_p\lambda_w}{8\pi(1+\delta)\rho_0^2}[\beta_y + k_w^2\beta_y^2 J_y + ...], \tag{12.1}$$

where β_y is the average beta function at the wiggler, J_y is the action, and ρ_0 is the bending radius of the peak field B_0. The nonlinear tune shift can also be computed numerically using the differential algebra [17] and the normal-form analysis [18]. The numerical results are tabulated in Table 5 for the new damping ring with two different models of wiggler. The only change of $\partial\nu_y/\partial\epsilon_y$ in the table can be compared with the contribution from the second term in Eq. (12.1). Of course one has to take the number of wigglers $N_w = 112$ and $\beta_y = 12$ m into account. The agreement is within a few percent.

wiggler model:	linear	single-mode
$\partial\nu_x/\partial\epsilon_x$	-1583	-1583
$\partial\nu_x/\partial\epsilon_y$,$\partial\nu_y/\partial\epsilon_x$	-320	-320
$\partial\nu_y/\partial\epsilon_y$	-860	$+2609$

Table 5: *Nonlinear tune shifts in the new dogbone damping ring. Here $\epsilon_{x,y}$ are the emittance of the beam ($\epsilon_{x,y} = 2J_{x,y}$).*

The dynamic aperture of both dogbone lattices with the single-mode wigglers are plotted in Fig. 10. Compared with Fig. 8, one can see that the single-mode wigglers made little decrease in the dynamic aperture in the

vertical plane for the new dogbone lattice. However for the old one, the degradation is more pronounced, presumably due to an excited resonance near its working point.

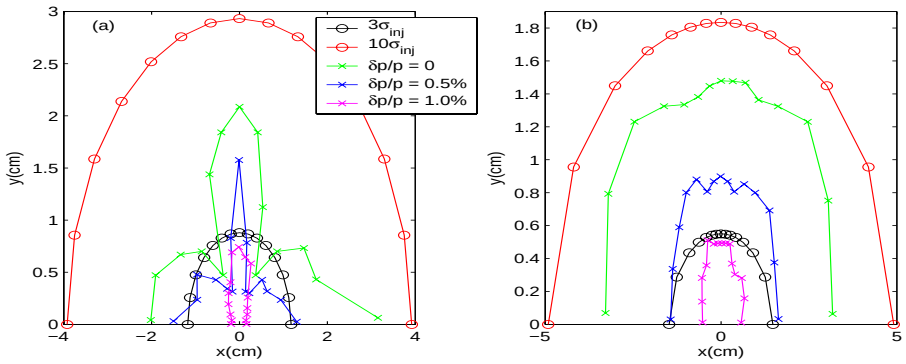

Figure 10: *Dynamic apertures of both dogbone damping rings with single-mode wigglers: a) DESY's design b) SLAC's new design.*

13 Field due to pole width

For a realistic wiggler with a finite pole width, we have $B_x \neq 0$. In addition to the intrinsic field described by Eq. (10.1), we need the harmonic expansion [19]:

$$\begin{aligned}
B_x &= \sum_{n=1}^{N_{sy}} \sum_{m=1}^{N_y} B_x^{(n,m)} \sinh(k_x^{n,m} x) \sin(k_y^{(m)} y) \sin(k_s^{(n)} s + \phi_x^{(n,m)}), \\
B_y &= \sum_{n=1}^{N_{sy}} \sum_{m=1}^{N_y} B_y^{(n,m)} \cosh(k_x^{n,m} x) \cos(k_y^{(m)} y) \sin(k_s^{(n)} s + \phi_x^{(n,m)}), \\
B_s &= \sum_{n=1}^{N_{sy}} \sum_{m=1}^{N_y} B_s^{(n,m)} \cosh(k_x^{n,m} x) \sin(k_y^{(m)} y) \cos(k_s^{(n)} s + \phi_x^{(n,m)}),
\end{aligned} \tag{13.1}$$

where $B_y^{(n,m)} = k_y^{(m)} B_x^{(n,m)} / k_x^{(n,m)}$, $B_s^{(n,m)} = k_s^{(n)} B_x^{(n,m)} / k_x^{(n,m)}$, $k_y^{(m)} = m\pi/h$, $k_x^{(n,m)} = \sqrt{k_s^{(n)} + k_y^{(m)}}$, and the h is the height of the pole. It is easy to see from Eq.(13.1) that $B_x(x, h, s) = 0$, which implies that the magnetic field

enters perpendicular into the pole. It is not hard to show that its vector potential, in the axial gauge $A_s = 0$, is given by

$$\begin{aligned} A_x &= \sum_{n=1}^{N_{sy}} \sum_{m=1}^{N_y} A_x^{(n,m)} \cosh(k_x^{n,m} x) \cos(k_y^{(m)} y) \cos(k_s^{(n)} s + \phi_x^{(n,m)}), \\ A_y &= \sum_{n=1}^{N_{sy}} \sum_{m=1}^{N_y} A_y^{(n,m)} \sinh(k_x^{n,m} x) \sin(k_y^{(m)} y) \cos(k_s^{(n)} s + \phi_x^{(n,m)}), \quad (13.2) \end{aligned}$$

where $A_x^{(n,m)} = -k_y^{(m)} B_x^{(n,m)} / k_x^{(n,m)} k_s^{(n)}$ and $A_y^{(n,m)} = B_x^{(n,m)} / k_s^{(n)}$.

A map of the three-dimensional field in a quarter period of the wiggler was obtained using a magnetic design code for the DESY's dogbone damping ring. The field map includes all three components: B_x, B_y, and B_s on a grid of $11 \times 11 \times 51$ with cubic dimension: 1 mm×1 mm×2 mm. We fit all data points in the field map with the superposition of the intrinsic and pole-width field in Eqs. (10.1) and (13.1). The residual of the fitting in rms is reduced to a few Gauss. Here, we show the residual of B_y in the x-z planes at $y = 0, 6$ mm in Fig. 11. The peak field $B_0 = 1.68$ T is reached at $z = 100$ mm in the field map.

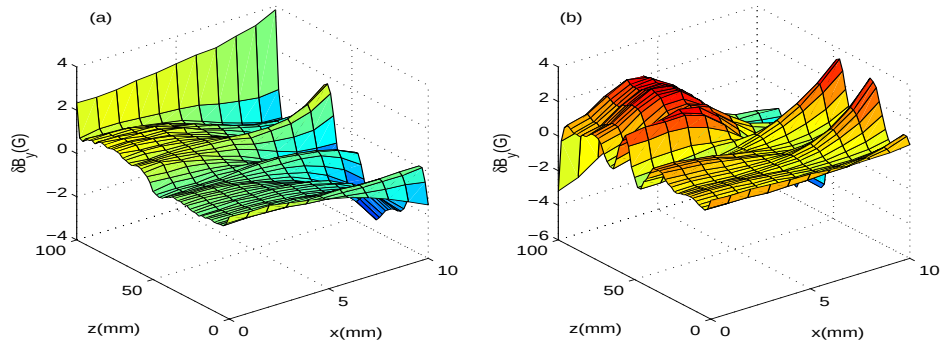

Figure 11: *Residual of fitting to a three-dimensional field map. a) B_y in x-z plane at $y = 0$ and b) $y = 6$ mm.*

There are 44 modes, with each mode having two free parameters, used in the fitting. The wiggler parameters used are $\lambda_w = 0.4$ m and $h = 0.025$ m. It can be seen from plot (b) that there is a bump near the pole, which is largely due to the field saturation. One can always reduce the residual further by introducing other types of harmonic expansions [20] or more terms in the field expansions. But that could significantly slow down the tracking.

14 A hybrid integrator

For a wiggler with finite pole width, $e^{-:H_2:\Delta s/2}$ in Eq. (11.3) can not be solved explicitly. Some kind of approximation is required. Here we introduce a mix-variable generating function:

$$F_2 = \sum_{i=1}^{3} q_i \bar{p}_i + H(q, \bar{p})\Delta s, \tag{14.1}$$

to make a canonical transformation:

$$\begin{aligned} \bar{q}_i &= \frac{\partial F_2}{\partial \bar{p}_i} = q_i + \frac{\partial H(q,\bar{p})}{\partial \bar{p}_i}\Delta s, \\ p_i &= \frac{\partial F_2}{\partial q_i} = \bar{p}_i + \frac{\partial H(q,\bar{p})}{\partial q_i}\Delta s. \end{aligned} \tag{14.2}$$

In general, these equations can only be solved numerically. It is commonly referred as the inexplicit integration. However for some special forms of Hamiltonian H, such as H_2 which has linear dependency upon p_x and p_y, they can be solvable analytically. For the Lie transformation: $e^{:-H_2:\Delta s}$, with a substitution of $H = -(p_x a_x + p_y a_y)/(1+\delta)$ into Eq. (14.2) and simple algebra, we obtain

$$\begin{aligned} \bar{x} &= x - \frac{a_x}{1+\delta}\Delta s, \\ \bar{p}_x &= [(1 - \frac{\partial_y a_y}{1+\delta}\Delta s)p_x + \frac{\partial_x a_y}{1+\delta}\Delta s p_y]/\det, \\ \bar{y} &= y - \frac{a_y}{1+\delta}\Delta s, \\ \bar{p}_y &= [\frac{\partial_y a_x}{1+\delta}\Delta s p_x + (1 - \frac{\partial_x a_x}{1+\delta}\Delta s)p_y]/\det, \\ \bar{\delta} &= \delta, \\ \bar{l} &= l - \frac{(\bar{p}_x a_x + \bar{p}_y a_y)}{(1+\delta)^2}\Delta s, \end{aligned} \tag{14.3}$$

where

$$\det = 1 - \frac{(\partial_x a_x + \partial_y a_y)\Delta s}{1+\delta} + \frac{\partial_x a_x \partial_y a_y \Delta s^2}{(1+\delta)^2}. \tag{14.4}$$

To be precise, this approximation is only a first-order integrator. However, in this particular application to a realistic wiggler, it is a pretty good approximation since the intrinsic potential in Eq. (10.3) dominates the total

expansion; also, for the intrinsic potential alone, this first-order integrator becomes the exact solution.

The transformation defined by Eq. (14.3) is also symplectic since it originated from a canonical transformation. Of course, it is not so hard to show its symplecticity directly. In addition, this hybrid integrator, starting from an inexplicit scheme and ending up with an explicit solution, allows us to extract a nonlinear map of an arbitrary order by simply tracking the truncated power series as if it were an explicit symplectic integrator.

15 Dynamic aperture with realistic wigglers

After we implemented these integration schemes in LEGO, we used the fitted vector potential in the 44-mode expansion presenting the wigglers and computed the dynamic aperture of the DESY's dogbone damping ring. The dynamic aperture for the on-momentum particles was reduced significantly to 1-2σ_{inj}. This result, shown in Fig. 12, indicates that there could be too much loss during the injection of positrons. Similar results were obtained separately by Venturini [21] and Urban [22] using different presentations of field, integration methods, and tracking codes.

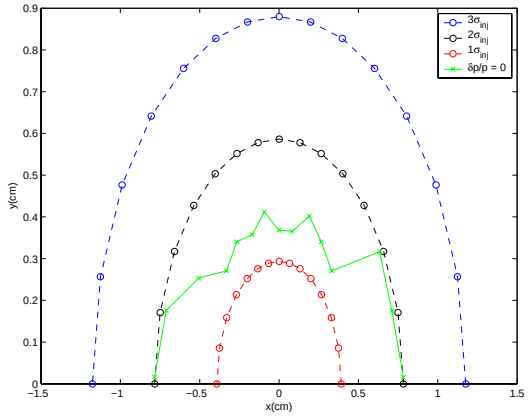

Figure 12: *Dynamic aperture of DESY's dogbone damping ring with realistic wigglers.*

Actually, the insufficient dynamic aperture of DESY's ring was the main motivation for us to initiate our study of a new design. We have not completely solve the problem because the dynamic aperture with the full nonlinear wigglers in the newly designed dogbone damping ring is about the same

as shown in Fig. 12. That is not too surprising since the good field region of the wigglers is so small that the 450-meter long wigglers acted as if they were physical collimators.

Obviously, the wiggler's nonlinear field has to be significantly reduced to achieve an adequate acceptance in the damping ring. Given how little impact on the dynamic aperture in the newly designed dogbone damping ring by the single-mode wigglers shown in plot (b) of Fig. 10. There should be a good and realistic design of a wiggler that could satisfy our stringent requirement on the acceptance. A further study is needed to make a reasonable and achievable specification of the wigglers.

16 Conclusion

The hybrid integrator developed in this paper is symplectic and very general. It can also be applied to the integration of the fringe field at the end of a magnet. Compared with the conventional explicit integrator [23], it is much simpler and therefore faster in tracking. In addition, it retains an important property: obtaining a high-order map using the differential algebra. The integration method developed in this paper is fully self-consistent. It allows us to study the effects of misalignment inside the wiggler with a nonlinear field.

It is very encouraging to see almost the same degraded dynamic aperture when the same field map of the wiggler and the dogbone lattice are applied by several authors using different methods of tracking. Our work on the single-mode wiggler has demonstrated that the degradation by the damping wigglers is not a fundamental limitation of the lattices and it is solvable with more engineering efforts.

We have designed two new damping rings: compact and dogbone, based on the π cell and non-interlaced sextupoles. We believe that their acceptances will be adequate once their damping wigglers are improved in terms of the field quality. The chromatic effects in these rings are under further optimization. A realistic specification of wigglers and analysis of lattice tolerance remain to be carried out in addition to the study of space-charge effects and the coupling bumps.

Acknowledgments

I would like thank Gordon Bowden, Yuri Nosochkov, Tor Raubenhemier, Andy Wolski, Yiton Yan for many helpful discussions. This work was supported by the Department of Energy under Contract Number: DE-AC02-76SF00515.

References

[1] W. Decking, "Optical Layout of the TESLA 5 Gev Damping Ring," TESLA 2001-11, (2001).

[2] L.C. Teng, "Minimizing the Emittance in Designing the Lattice of an Electron Storage Ring," Fermilab Report No. TM-1269, (1984).

[3] "Zeroth-Order Design Report for the Next Linear Collider," LBNL-PUB-5424, SLAC Report 474, UCRL-ID-12461, (1996).

[4] A. Wolski, "Lattices with Large Dynamic Aperture for ILC Damping Rings," LBNL-57045, CBP Tech Note-331, (2005).

[5] P. Emma and T. Raubenhemier, "Systematic approach to damping ring design," Phys. Rev. ST, Accel. and Beams, **4**, 021001, (2001).

[6] A. Xiao, "An Alternative TESLA Damping Ring Lattice Design at Fermilab," Techical Report, (2004).

[7] M. Donald, *et al.*, "Lattice Design for the High Energy Ring fo the SLAC B-Factory," SLAC-PUB-6873, (1995).

[8] Y. Cai, *et al.*, "Low Energy Ring Lattice of the PEP-II Asymmetric B-Factory," SLAC-PUB-6868, Proceedings of PAC95, p.576, (1995).

[9] H. Grote and F.C. Iselin, "The MAD Program," CERN Report No. CERN/SL/90-13 (AP) Rev. 4, (1994).

[10] "PEP-II: An Symmetric B Factory," Conceptual Design Report, SLAC-418, (1993).

[11] "KEKB B-Factory Design Report," KEK Report 95-7, (1995).

[12] Y. Cai, M. Donald, J. Irwin, Y. Yan, "LEGO: A Modular Accelerator Design Code," SLAC-PUB-7642, (1997).

[13] K.L. Brown, IEEE Trans. Nucl. Sci. NS-26, 3490 (1979).

[14] H. Koiso, "Lattice Design of the KEK B-Factory Rings," SLAC-Report, SLAC-400, p86 (1992).

[15] R. Ruth, "Single-Particle Dynamics in Circular Accelerators," AIP Conference Proceedings No. 153, Vol.1 p166, M. Month and M. Dienes editors (1985).

[16] E. Forest, J. Bengtsson, M. F. Reusch, "Application of the Yoshida-Ruth techniques to implicit integration and multi-map explict integration," Phys. Lett. A **158**, p99 (1991).

[17] M. Berz, "Differential Algebra Description of Beam Dynamics to Very High Order," Part. Accel. **24**, 109 (1989).

[18] E. Forest, M. Berz, and J. Irwin, "Normal Form Methods for Complicated Periodic Systems: A Complete Solution Using Differential Algebra and Lie Operators," Part. Accel. **24** 91 (1989).

[19] K. Halbach, "Scalar Potential for 3D Field in 'Business Region' of Insertion Device with Finite Width Poles," LBL Report, FEB-A95, (1992).

[20] D. Sagan, J.A. Crittenden, D. Rubin, E. Forest, "A Magnetic Field Model for Wigglers and Undulators," Proceedings, PAC03, (2003).

[21] M. Venturini, Presented at ILC Americas Workshop, SLAC, November 2004.

[22] J. Urban, Presented at ILC teleconference meeting, March 2005.

[23] Y.K. Wu, E. Forest, D.S. Robin, "Explicit symplectic integrtor for s-dependent static magnetic field," Phys. Rev. E **68** 046502 (2003).